



Research Paper

Prevent thermal runaway of lithium-ion batteries with minichannel cooling

Jian Xu^a, Chuanjin Lan^a, Yu Qiao^b, Yanbao Ma^{a,*}^a School of Engineering, University of California, Merced, Merced, CA 95343, USA^b Department of Structural Engineering, University of California San Diego, La Jolla, CA 92093, USA

HIGHLIGHTS

- A 3D model was developed to study nail penetration induced thermal runaway.
- Effects of flow rate, thermal abuse reactions, and nail dimensions were examined.
- Minichannel cooling at cell level cannot cease thermal runaway in a single cell.
- Minichannel cooling can prevent thermal runaway propagation between cells.

ARTICLE INFO

Article history:

Received 14 April 2016

Revised 14 August 2016

Accepted 23 August 2016

Available online 24 August 2016

Keywords:

Electric vehicle
Lithium ion battery
Thermal management
Thermal runaway
Nail penetration
Minichannel cooling

ABSTRACT

Thermal management on lithium-ion batteries is a crucial problem for the performance, lifetime, and safety of electric vehicles (EVs) and hybrid electric vehicles (HEVs). Fire and explosions can be triggered by thermal runaway if the temperature of the lithium-ion batteries is not maintained properly. This work describes a minichannel cooling system designed at the battery module level and the investigation on its efficacy on the mitigation of thermal runaway. Nail penetration was employed to simulate the internal short circuits, which in reality may be caused by vehicle collisions and/or manufacturing defects. Two integrated models were utilized to study thermal runaway: the conjugate heat transfer model and the reaction kinetics model. Numerical simulations were conducted to understand the thermal runaway process and the effects of flow rate, thermal abuse reactions, nail penetration depth, and nail diameter. It is concluded that minichannel cooling at cell level cannot cease thermal runaway in a single cell, but it can prevent battery fratricide due to thermal runaway propagation between cells.

© 2016 Elsevier Ltd. All rights reserved.

1. Introduction

The rapid emergence of various electric vehicles (EV) and hybrid electric vehicles (HEV) around the world has created an urgent demand for high-performance batteries at low cost. Lithium-ion batteries are commonly used in EVs, due to their high energy density [1–3]. Their lifetime, performance, and safety are largely influenced by the operating battery temperature [4–6]. At a temperature below the desired range (15–35 °C [7]), battery performance will be lowered due to poor ion transport. At a temperature higher than 35 °C, side reactions happen faster, which leads to higher loss rates of cyclable lithium and active materials [7]. Many thermal management methods, e.g., air cooling [8–14], refrigerant cooling [15,16], liquid cooling [13,17–19], and phase

change material (PCM) cooling [20–23], have been investigated. Though a few thermal management schemes are being applied in commercial electric cars (e.g. air cooling: Toyota Prius, Nissan Leaf; refrigerant cooling: BMW i3; and liquid cooling: Tesla Model S, Chevy Volt), after and more cost-effective thermal management methods are still desirable, especially in extreme environments or under abuse conditions that would otherwise lead to a fire or explosion [24–26].

When the temperature of a lithium-ion battery is elevated and the heat can't be dissipated effectively, thermal runaway due to the exothermic reactions can occur [2,25,26]. Thermal runaway involves a rapid temperature increase, release of gas, smoke, fire, and an explosion. There are numerous external and internal abuse conditions that can cause thermal runaway, e.g., external heating, over charging/discharging, nail penetration, and external short [27]. Among them, nail penetration is often used to simulate the internal short circuit in a cell [28,29], analogue to the internal shorting resulted from car collisions or manufacturing defects such

* Corresponding author.

E-mail address: yma5@ucmerced.edu (Y. Ma).

Nomenclature

A	surface area of the inserted nail (mm^2)	W	specific content in jellyroll (kg/m^3)
a	frequency factor (1/s)	w	width of the minichannel (mm)
c	dimensionless concentration	z	dimensionless solid electrolyte interface (SEI) thickness
c_p	specific heat ($\text{J}/\text{kg K}$)	α	degree of conversion
E	activation energy (J/mol)	ε	emissivity of the battery surface
H	heat release during thermal abuse (J/kg)	ρ	density (kg/m^3)
h	height of the minichannel (mm)	σ	Stefan-Boltzmann constant, $5.67\text{e}-8$ ($\text{W}/\text{m}^2 \text{K}^4$)
h_{conv}	convective heat transfer coefficient ($\text{W}/\text{m}^2 \text{K}$)	μ	dynamic viscosity ($\text{kg}/\text{m s}$)
k	thermal conductivity ($\text{W}/\text{m K}$)	δ	thickness of aluminum between the outer surface and the minichannel (mm)
L	depth of nail penetration (mm)		
P	pressure (Pa)		
ΔP	total pressure drop across the minichannel system (Pa)		
\dot{q}_{conv}	convective heat transfer at the cell boundaries (W/m^2)	Subscripts	
\dot{q}_{rad}	radiative heat transfer at the cell boundaries (W/m^2)	<i>abuse</i>	thermal abuse
Q	pumping power (W)	<i>amb</i>	ambient
R	the gas constant, 8.314 ($\text{J}/\text{mol K}$)	<i>b</i>	battery
r	radius of the nail (mm)	<i>e</i>	electrolyte
S	heat generation during nail penetration (W/m^3)	<i>n</i>	nail
T	temperature (K)	<i>ne</i>	negative-electrolyte
t	time (s)	<i>pe</i>	positive-electrolyte
\bar{u}	velocity (m/s)	<i>sei</i>	solid electrolyte interface
V	volume of the inserted nail (mm^3)	<i>sur</i>	battery boundaries
\dot{V}	volumetric flow rate (m^3/s)	<i>w</i>	water

as a conductive particle wound in the jelly roll. It has been commonly believed that during the nail penetration process, short circuit occurs first between adjacent electrode pairs, which generates a huge amount of heat and increases the battery temperature. When the battery temperature reaches a threshold (~ 120 °C), the decomposition of battery materials (referred to as thermal abuse) takes place, which further accelerates the heat generation [30,31]. Hatchard et al. [32] conducted oven exposure tests for cylindrical and prismatic Li-ion cells, and developed a 1D modeling approach to calculate the reaction kinetics for thermal abuse. This modeling method was then extended by Kim et al. [33] to 3D so that the geometrical features of the battery could be considered. Zhao et al. [34] used a 3D multiscale electrochemical-thermal model to conduct a parametric study of the nail penetration process in a large-format li-ion cell. Using this model, they analyzed the effects of nail diameter, nail conductivity, and cell capacity on the cell behavior.

As the thermal runaway is triggered in a single cell, it may propagate to adjacent cells if no appropriate measurement is used to prevent it. The thermal runaway propagation could result in a severe thermal hazard, and therefore, should be considered in battery thermal management design [35]. At present, however, only limited experimental and computational studies have been conducted to study the mechanism during this propagation process. To the best knowledge of the authors, the only experimental study in literature was conducted by Feng et al. [29]. They investigated the penetration induced thermal runaway propagation within a 6-battery module. The first battery of the module was penetrated to trigger the thermal runaway. Their results showed that 12% of the total heat released in thermal runaway could trigger the thermal runaway of the adjacent battery. Yang et al. [36] developed a 3D electrochemical-electrical-thermal model using National Renewable Energy Laboratory (NREL)'s Multi-Scale-Multi-Dimensional (MSMD) modeling approach to identify the characterization of thermal runaway propagation in a li-ion battery module. Chen et al. [37] implemented a coupled electro-thermal model in COMSOL Multiphysics to study the influence of the overheated cylindrical battery cell on surrounding batteries in the 7×3

battery module. Only the convective and radiative heat transfer on the battery surface was used to dissipate the heat generated in the batteries. Their results showed that thermal runaway can be induced in other adjacent cells within a 3 mm distance of the overheated cell if the accumulated heat could not be dissipated sufficiently rapidly.

In this study, a novel minichannel cooling system was developed for the thermal management of the lithium-ion battery module. The minichannel design features multiple aluminum multi-port extrusions. Coolant will flow through the minichannels and absorb the heat from the batteries. This design has the advantage of high efficiency, light weight, and low cost. Our goal is to investigate the characteristics of nail penetration induced thermal runaway with the assist of the minichannel cooling system at the battery cell level and battery module level. The feasibility of using minichannel cooling to prevent thermal runaway in one battery cell and thermal runaway propagation from one cell to adjacent cells is also analyzed.

2. Model description

2.1. Physical problem

The novel minichannel cooling system is designed based on a battery module with five prismatic cells, as shown in Fig. 1. The dimensions of each cell are 180 mm (height) by 130 mm (width) by 50 mm (depth), and the capacity is 55 Ah. Three of the five cells are wrapped by aluminum minichannels. The geometric details of the minichannel are shown in Fig. 2. The height of channel is $h = 3$ mm, and width is $w = 3$ mm. The thickness of aluminum between the outer surface and channel is $\delta = 1$ mm, and the thickness between two neighbor channels is 2δ [1,38]. This particular minichannel geometry is adopted from a typical extruded multi-port aluminum tube. The changes to the geometry will have impact on its performance. For example, if the channel height (h) is reduced while other parameters remain the same, the liquid flow rate will increase and therefore the minichannel system will have

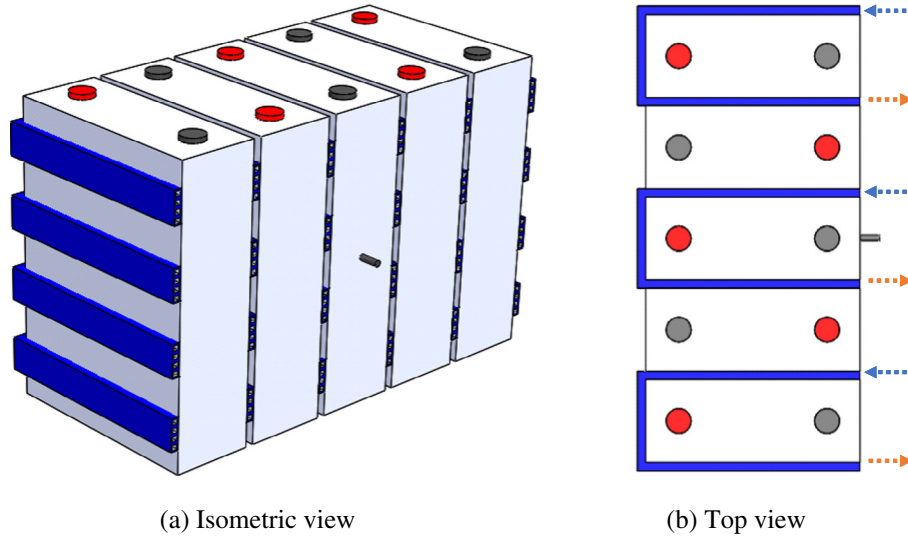


Fig. 1. Schematic of the minichannel cooling system and the nail penetration location. Blue arrows indicate flow inlet, and orange arrows represent flow outlet. (For interpretation of the references to colour in this figure legend, the reader is referred to the web version of this article.)

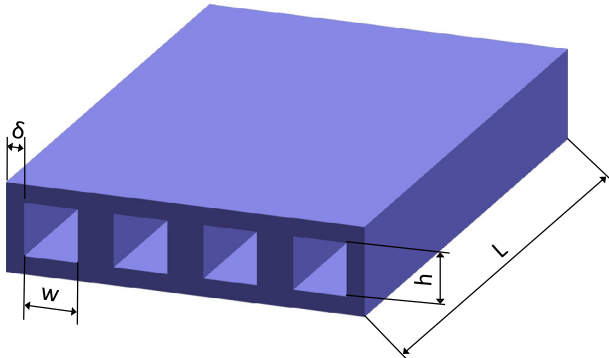


Fig. 2. Details of the minichannel geometry.

a better cooling performance. However, the pressure drop will also increase. A study to optimize the minichannel geometry is currently underway.

When the nail penetration occurs, energy is released at an extremely high rate (in the order of 10^7 W/m^3), which results in dramatic temperature increase in a short time period. This complex process consists of two major mechanisms: the short circuit, which takes place at the nail-battery interface, and the thermal abuse caused by the decomposition of the jelly-roll materials in the whole battery cell. In this study, a 3 mm (diameter) by 40 mm (length) nail is supposed to be inserted into the middle cell at the center of its side surface, as shown in Fig. 1. The feasibility of using minichannel cooling to prevent the thermal runaway of a single cell triggered by nail penetration and the thermal runaway propagation from one cell to its neighboring cells was investigated in this study.

2.2. Governing equations of the minichannel flow

Liquid water is applied as the cooling medium inside the aluminum minichannels, and the flow is kept in laminar regime. The governing equations for the water [1] are:

$$\frac{\partial(\rho_w)}{\partial t} + \nabla \cdot (\rho_w \vec{u}) = 0 \quad (1)$$

$$\frac{\partial(\rho_w \vec{u})}{\partial t} + \nabla \cdot (\rho_w \vec{u} \vec{u}) = -\nabla P + \mu \nabla^2 \vec{u} \quad (2)$$

$$\frac{\partial(\rho_w c_{p,w} T_w)}{\partial t} + \nabla \cdot (\rho_w c_{p,w} \vec{u} T_w) = \nabla \cdot (k_w \nabla T_w) \quad (3)$$

2.3. Energy balance of the battery cell

The energy conservation equation of battery is given as follows:

$$\frac{\partial(\rho_b c_{p,b} T_b)}{\partial t} = \nabla \cdot (k_b \nabla T_b) + S \quad (4)$$

Due to the lithium-ion battery's multi-layered structure, the anisotropic thermal conductivity of the battery (through-plane vs. in-plane) is considered. The material properties of the battery as well as those of the aluminum minichannel and the nail are shown in Table 1. S is the heat generation during the nail penetration process. The overall heat generation process is divided into two stages. In stage I, the heat is only generated at the nail-cell interface caused by short circuiting immediately after the nail penetration. The heat generation rate of stage I is adopted from Ref. [31]. The heat generated leads to a dramatic increase of the battery temperature. When the temperature exceeds the threshold ($\sim 120 \text{ }^\circ\text{C}$), it will trigger the decomposition of the jelly-roll materials and start the stage II heat generation. In the second stage, the heat generation is modeled as a distribution of volumetric heat source within the whole cell. More details about the stage II heat generation are shown in Section 2.4.

During the cooling of the battery cell, the heat is first conducted from the battery to the aluminum minichannels through the battery-minichannel interface, then from the minichannel to the fluid through convection, and finally dissipated by the cooling fluid. So the heat conduction rate at the battery-minichannel interface has a significant impact on the total cooling efficiency. The thermal conductance through the contact interface is determined by the contact pressure, the microhardness of the softer material,

Table 1
Material properties.

Parameter	Aluminum minichannel	Nail	Battery [32]
k (W/(m K))	238	44.5	3.4 (through-plane) 34.0 (in-plane)
ρ (kg/m ³)	2700	7850	1700
c_p (J/(kg K))	900	475	830

the surface roughness, and the surface roughness slope. In this study, thermal grease is assumed to be applied at the interface, and an average thermal conductance of $3 \times 10^4 \text{ W}/(\text{m}^2 \text{ K})$ is adopted [39].

The convective and the radiative heat transfer at the cell boundaries are also considered to account for the heat exchange between the system and the ambient. They are governed by Eqs. (5) and (6). Natural convection and radiation from gray diffuse surfaces are assumed in this study, and an average h value of $7 \text{ W}/(\text{m}^2 \text{ K})$ and an average ε of 0.8 are adopted from Ref. [33].

$$\dot{q}_{conv} = h_{conv}(T_{sur} - T_{amb}) \quad (5)$$

$$\dot{q}_{rad} = \varepsilon\sigma(T_{sur}^4 - T_{amb}^4) \quad (6)$$

2.4. Thermal abuse model

The thermal abuse model considers four reactions during the decomposition of jelly-roll materials. They are: the solid electrolyte interface (SEI) decomposition reaction, the negative-electrolyte reaction, the positive-electrolyte reaction, and the electrolyte decomposition reaction. The rates of these reactions are expressed in Arrhenius form, and are functions of the battery temperature and battery material properties. The required physical and kinetic parameters and initial values for the thermal abuse model are shown in Table 2.

$$S_{abuse} = S_{sei} + S_{ne} + S_{pe} + S_e \quad (7)$$

(I) SEI decomposition

$$S_{sei}(T, c_{sei}) = H_{sei} W_{sei} a_{sei} \exp\left(\frac{-E_{sei}}{RT}\right) c_{sei} \quad (8)$$

$$\frac{dc_{sei}}{dt} = -a_{sei} \exp\left(\frac{-E_{sei}}{RT}\right) c_{sei} \quad (9)$$

(II) Negative-electrolyte reaction

$$S_{ne}(T, c_{ne}, z) = H_{ne} W_{ne} a_{ne} \exp\left(\frac{-z}{z_0}\right) \exp\left(\frac{-E_{ne}}{RT}\right) c_{ne} \quad (10)$$

$$\frac{dc_{ne}}{dt} = -a_{ne} \exp\left(\frac{-z}{z_0}\right) \exp\left(\frac{-E_{ne}}{RT}\right) c_{ne} \quad (11)$$

Table 2
Physical and kinetic parameters and initial values for thermal abuse model obtained from Refs. [31–33].

Symbol	Value	Description
H_{sei}	$2.57 \times 10^5 \text{ (J/kg)}$	SEI-decomposition heat release
W_{sei}	$6.104 \times 10^2 \text{ (kg/m}^3\text{)}$	Specific carbon content in jellyroll
a_{sei}	$1.667 \times 10^{15} \text{ (1/s)}$	SEI-decomposition frequency factor
E_{sei}	$1.3508 \times 10^5 \text{ (J/mol)}$	SEI-decomposition activation energy
H_{ne}	$1.714 \times 10^6 \text{ (J/kg)}$	Negative-electrolyte heat release
W_{ne}	$6.104 \times 10^2 \text{ (kg/m}^3\text{)}$	Specific carbon content in jellyroll
a_{ne}	$2.5 \times 10^{13} \text{ (1/s)}$	Negative-electrolyte frequency factor
E_{ne}	$1.3508 \times 10^5 \text{ (J/mol)}$	Negative-electrolyte activation energy
H_{pe}	$3.14 \times 10^5 \text{ (J/kg)}$	Positive-electrolyte heat release
W_{pe}	$1.438 \times 10^3 \text{ (kg/m}^3\text{)}$	Specific positive active content in jellyroll
a_{pe}	$6.667 \times 10^{13} \text{ (1/s)}$	Positive-electrolyte frequency factor
E_{pe}	$1.396 \times 10^5 \text{ (J/mol)}$	Positive-electrolyte activation energy
H_e	$1.55 \times 10^5 \text{ (J/kg)}$	Electrolyte decomposition heat release
W_e	$4.069 \times 10^2 \text{ (kg/m}^3\text{)}$	Specific electrolyte content in jellyroll
a_e	$5.14 \times 10^{25} \text{ (1/s)}$	Electrolyte decomposition frequency factor
E_e	$2.74 \times 10^5 \text{ (J/mol)}$	Electrolyte decomposition activation energy
$c_{sei,0}$	0.15	Initial value of c_{sei}
$c_{ne,0}$	0.75	Initial value of c_{ne}
$c_{e,0}$	1	Initial value of c_e
z_0	0.033	Initial value of z
α_0	0.04	Initial value of α

$$\frac{dz}{dt} = a_{ne} \exp\left(\frac{-z}{z_0}\right) \exp\left(\frac{-E_{ne}}{RT}\right) c_{ne} \quad (12)$$

(III) Positive-electrolyte reaction

$$S_{pe}(T, c_{pe}) = H_{pe} W_{pe} a_{pe} \alpha (1 - \alpha) \exp\left(\frac{-E_{pe}}{RT}\right) \quad (13)$$

$$\frac{d\alpha}{dt} = a_{pe} \alpha (1 - \alpha) \exp\left(\frac{-E_{pe}}{RT}\right) \quad (14)$$

(IV) Electrolyte decomposition

$$S_e(T, c_e) = H_e W_e a_e \exp\left(\frac{-E_e}{RT}\right) c_e \quad (15)$$

$$\frac{dc_e}{dt} = -a_e \exp\left(\frac{-E_e}{RT}\right) c_e \quad (16)$$

2.5. Initial and boundary conditions

The initial temperatures of the battery, the cooling channels, the nail, and the inlet water are set at 27°C . At flow inlets, the velocity and temperature of water are assumed to be uniform and constant. For the flow outlet, a constant zero pressure is specified and an outflow boundary condition is used for energy equations.

2.6. Numerical method

The multi-physics problem including fluid dynamics, heat transfer, and chemical reaction was solved in COMSOL Multi-physics. A 3D thermal model was developed to simulate the conjugate heat transfer between the battery, the minichannel, and the cooling fluid. A 1D PDE model was employed to calculate the heat generation due to thermal abuse. The two models were coupled in thermal balance of the cells, and were solved using finite element method. The liquid properties were set to be temperature dependent and determined by the material library embedded in COMSOL. After the model was built, the grid independence study was conducted to verify the accuracy of the modeling results. It was found that the results were to be repeatable within 3% when the mesh number was doubled.

2.7. Model validation

In our previous study [1], the simulation of heat transfer and laminar flow has been validated by checking the energy conservation and comparing the pressure drop through the whole minichannel with empirical equations. To validate the thermal abuse model, we imitated Hatchard's oven exposure test for a 18650 LiCoO₂/graphite cell [32]. In their experiment, a standard 18650 cylindrical cell was placed in an oven with constant temperature. Because of the high oven temperature (in the range of $130\text{--}160^\circ\text{C}$), thermal abuse will be triggered in the battery. As a result, the battery temperature will increase rapidly. After the temperature reaches the maximum, it will start to decrease due to the depletion of the materials in the battery. Fig. 3 shows the comparison of the modeling results with their experimental results for the case with oven temperature at 150°C . A very good agreement could be seen between the modeling results and their experimental results.

3. Results and discussions

3.1. Thermal runaway in a single cell

The feasibility of using minichannel cooling to prevent thermal runaway in a single cell is first studied. The computational domain

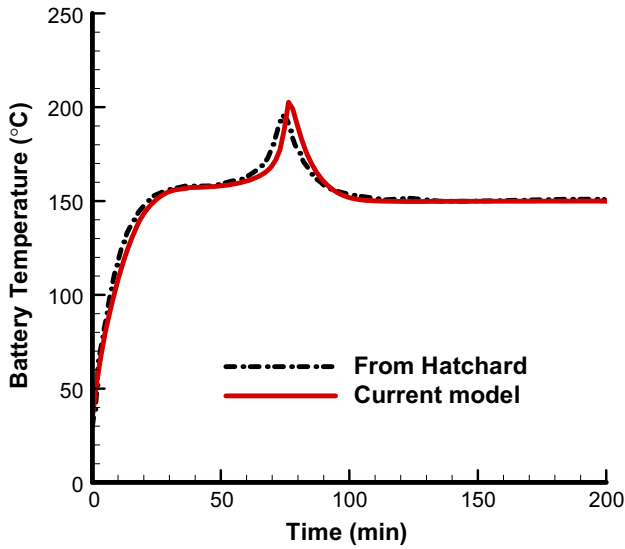


Fig. 3. Comparison of the results from current model with those from Hatchard et al. [32].

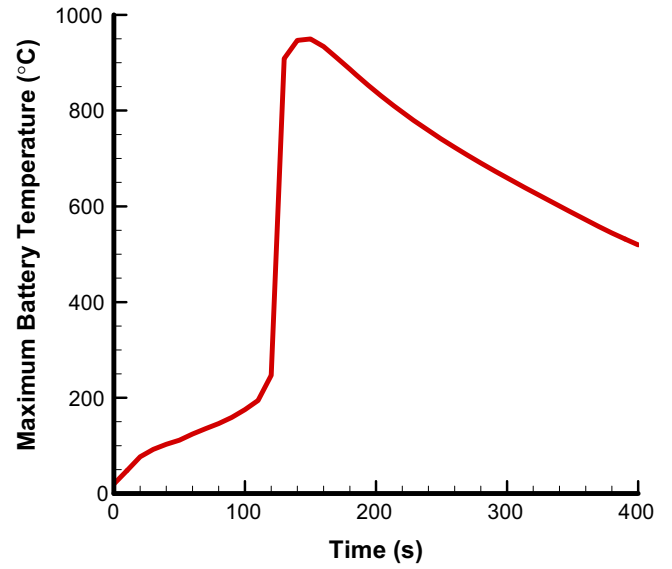


Fig. 5. Profile of the maximum temperature within the battery during nail penetration process, without cooling.

is shown in Fig. 4. To examine the performance of the minichannel cooling system, a case without liquid cooling is first investigated. The profile of the maximum temperature within the battery is shown in Fig. 5. The maximum temperature of the battery is monitored throughout the thermal runaway process, because once any point of the battery reaches the threshold temperature, the thermal abuse will be triggered locally and spread to the whole battery rapidly. In Fig. 5, the maximum temperature increases steadily in the first stage due to the heat generation caused by short circuit on the nail-cell interface. After the temperature exceeds 120 °C, the temperature starts to increase rapidly because of the thermal abuse and peaks around 950 °C at 150 s. When the jelly-roll materials are depleted, the temperature starts to decrease due to the heat loss at the battery boundaries.

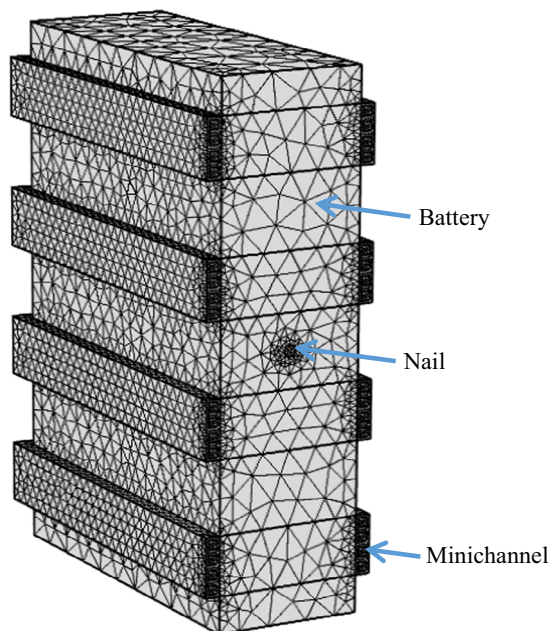


Fig. 4. The geometric model of thermal runaway caused by nail penetration.

3.1.1. Effect of flow rate

The cooling performance could be enhanced by increasing the flow rate. However, whether it is possible to prevent thermal runaway at high flow rate is undetermined. In this section, the effect of the flow rate on the battery cooling during nail penetration induced thermal runaway is studied. The results for the maximum temperatures of the battery and the water are shown in Fig. 6. For flow rate 0.1 L/min and 1.0 L/min, the maximum water temperature is larger than the boiling point (100 °C). In the current simulation model, boiling is not considered. In a real situation, the boiling inside the minichannels can cause a huge local pressure increase, which can damage the minichannel cooling system. Therefore, the boiling process should be avoided. Fig. 6 shows that the water temperature can be maintained below the boiling point by increasing the flow rate. At 10 L/min, the maximum water temperature is 45 °C, which is much lower than the water boiling point. This flow rate will be used in the following studies. It can be seen that the

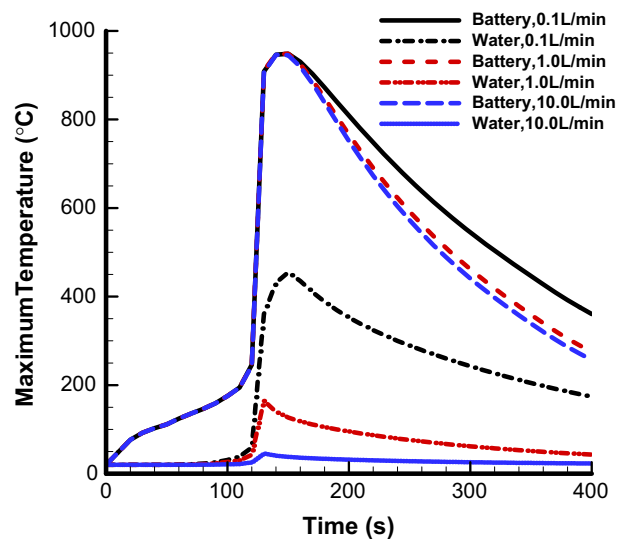


Fig. 6. Profiles of the maximum temperature of the battery and the water during nail penetration process at different flow rate.

thermal runaway can't be prevented even when the flow rate for a single cell is increased to 10.0 L/min. At different flow rates, the maximum battery temperature remains almost the same before the peak, and shows slight difference after that. This is because the heat generation due to thermal runaway is much larger than the heat dissipated by the fluid before the peak. After the peak, the thermal runaway diminishes due to the depletion of the jelly-roll materials and the heat dissipation due to minichannel cooling becomes more dominant.

When the flow rate increases, higher pumping power will be required. The pumping power Q is defined as shown in Eq. (17). This pumping power is the thermodynamic pumping power, which requires for a pump with 100% efficiency. The actual required pumping power would be higher due to pump inefficiency.

$$Q = \dot{V} \cdot \Delta P \quad (17)$$

The pressure drop and required pumping power for one battery cell at different flow rates are shown in Table 3. It can be seen that the minichannel cooling system requires very low pumping power. Even for 10.0 L/min flow rate, the required pumping power is only 1.3 W. When the flow rate increases from 0.1 L/min to 1.0 L/min and from 1.0 L/min to 10.0 L/min, the pressure drop increases by more than 20 times. As a result, the pumping power increases by more than 200 times.

Other liquid coolants, e.g. ethylene glycol and propylene glycol have also been studied, and the results are similar to the case of water due to the fact that the heat transfer is dominated by the thermal runaway process. Table 4 shows the comparison between the case of water and the case of ethylene glycol at 10.0 L/min flow rate. The maximum battery temperature is 955 °C for both cases. The maximum liquid temperature in the case of ethylene glycol is 7 °C higher because ethylene glycol has a lower specific heat than water. The pressure drop in the case of ethylene glycol, however, is about 6 times higher than that in the case of water due to much higher viscosity of ethylene glycol. As a result, much higher pumping power will be needed in the case of ethylene glycol.

3.1.2. Effect of thermal abuse reactions

The four heat generation rates of the thermal abuse reactions (S_{sei} , S_{ne} , S_{pe} , and S_e) are examined to study the detailed mechanisms during thermal runaway. The flow rate of 10.0 L/min is chosen for this study. The results are shown in Fig. 7. It can be seen that the SEI decomposition occurs first at 60 s when the temperature reaches 120 °C. Following that is the negative-electrolyte reaction, which takes place at around 80 s when the temperature increases to 150 °C. The positive-electrolyte reaction happens at 100 s when the temperature is 180 °C. Both the negative-electrolyte reaction and the positive-electrolyte reaction release huge amounts of heat. As a result, the battery temperature increases sharply. The electrolyte decomposition reaction takes places last, at 110 s, when the temperature reaches about 200 °C. At about 200 s, all the active materials are depleted.

3.1.3. Effects of the nail penetration depth and nail diameter

The simulations above are all for the case that the nail with 3 mm diameter will suddenly penetrate into the battery by 40 mm depth. In this study, the nail penetration depth and nail

Table 4

Comparison between different liquids at 10.0 L/min flow rate.

	Water	Ethylene glycol
Maximum battery temperature (°C)	955	955
Maximum liquid temperature (°C)	45	52
Maximum channel temperature (°C)	51	57
Pressure drop (Pa)	7.9e+3	4.8e+4
Pumping power (W)	1.3	8.1

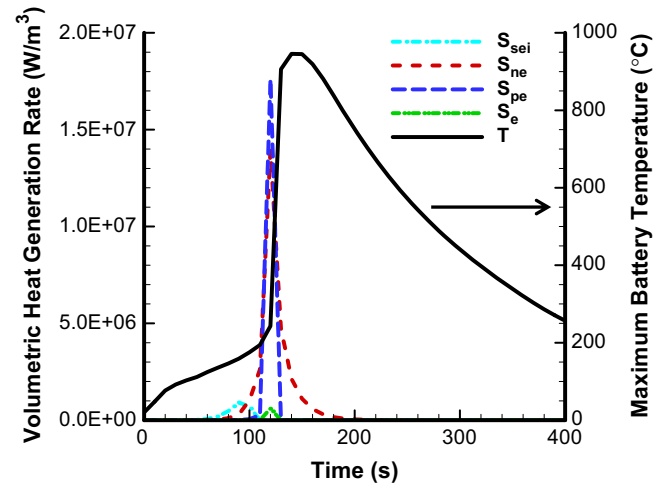


Fig. 7. Heat generation rates of thermal abuse reactions and the maximum battery temperature. The flow rate is 10.0 L/min.

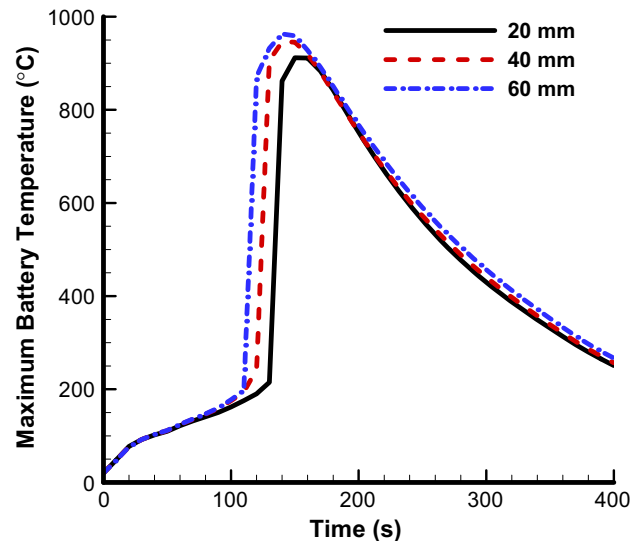


Fig. 8. Profiles of the maximum temperature within the battery at different nail penetration depth. The nail diameter is 3 mm. The flow rate is 10.0 L/min.

diameter will be varied to study the effects of the nail dimensions. The flow rate is fixed at 10.0 L/min.

Fig. 8 shows that when the penetration depth increases from 20 mm to 60 mm, the thermal runaway occurs at earlier stage and the battery reaches higher temperature. The effect of nail diameter is shown in Fig. 9. When the nail diameter increases from 3 mm to 5 mm, the thermal runaway takes place at much faster speed and the battery reaches higher temperature. The results in these two figures indicate that the increase of the surface area of the nail penetrated (either by increasing the nail penetration depth

Table 3

Comparison of pressure drop and pumping power at different flow rates for one battery cell.

Flow rate (L/min)	Pressure drop (Pa)	Pumping power (W)
0.1	1.3e+1	2.2e−5
1.0	3.0e+2	5.0e−3
10.0	7.9e+3	1.3

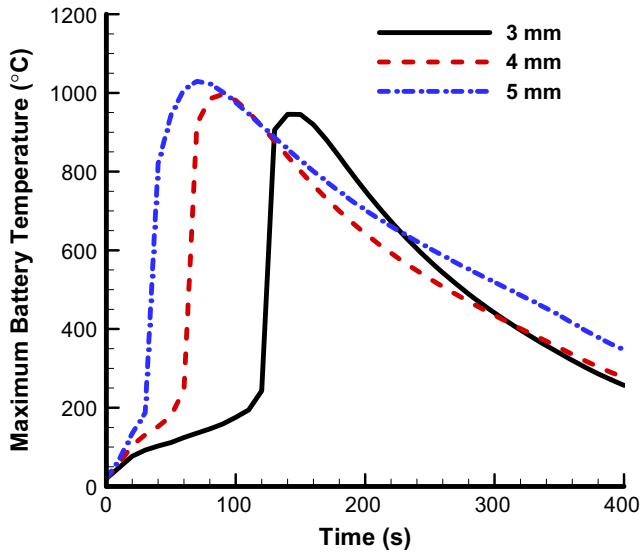


Fig. 9. Profiles of the maximum temperature within the battery at different nail diameter. The nail penetration depth is 40 mm. The flow rate is 10.0 L/min.

or by increasing the nail diameter) will cause a more severe and faster thermal runaway. This is because more heat will be generated over the nail surface due to short circuit.

3.2. Thermal runaway propagation from a cell to its neighboring cells

We have shown in the previous section that the minichannel cooling system could not prevent the thermal runaway of a battery cell even when the flow rate is as high as 10.0 L/min. However, whether it is possible for the minichannel cooling system to prevent the propagation of thermal runaway from one cell to its neighboring cells is unclear. This question will be studied in this section at the battery module level. Due to the asymmetry of the flow direction, the total battery module (as shown in Fig. 1) is simulated. In this section, battery 1 is used to represent the battery on which the nail penetration takes place, while battery 2 is the adjacent cell on the flow outlet side. Since the fluid is heated up during the process, the heat dissipation efficiency for the adjacent battery on the flow outlet side is reduced and therefore a higher maximum battery temperature will be expected.

The maximum temperature within battery 1 and battery 2 at different flow rates are shown in Fig. 10. The flow rates shown in the figure are only for a single cell rather than for the battery module. When the flow rate is 0.1 L/min, the thermal runaway on battery 2 is also triggered due to the heat transferred from battery 1. As a result, the maximum temperature of battery 2 reaches 800 °C. When the flow rate is increased to 10.0 L/min, the maximum temperature of battery 2 can be maintained below 60 °C. This indicates that a minichannel cooling system with independent control of the coolant flow rate for individual cells can prevent the propagation of thermal runaway from one cell to its neighboring cells by increasing the flow rate of the cell to 10.0 L/min. However, the control of the coolant flow rate is more often applied at the module level. In that case, a flow rate of 30.0 L/min (10.0 L/min × 3 cells) and a pumping power of 3.9 W (1.3 W × 3 cells) will be required to prevent the thermal runaway propagation from one cell to adjacent cells inside the injured battery module. At the battery pack level, about 80 battery modules of this kind will be needed to make an 85 kW h battery pack. To cool down the coolant of the whole pack after it is heated up by the batteries, a car radiator is assumed to be used. A conventional radiator is capable of cooling down up to

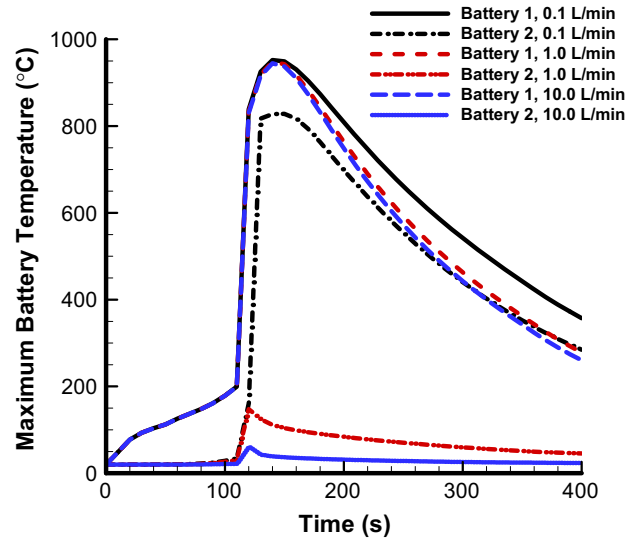


Fig. 10. Profiles of the maximum temperature within battery 1 and battery 2 at different flow rate.

200 L/min coolant [40]. This would be sufficient to cool down the coolant with 30.0 L/min flow rate for the injured battery module as well as the coolant with relatively low flow rate for the rest battery modules. If the control of the coolant flow rate can only be used at battery pack level, coolant with nearly 2400 L/min (30.0 L/min × 80 modules) flow rate and pumping power of 312 W (3.9 W × 80 modules) will be required when the thermal runaway on one battery cell is detected. This is infeasible because the flow rate is too high for a conventional radiator to cool down the coolant. In this case, some other techniques, e.g., the addition of multiwall carbon nanotube into battery electrodes to suppress both internal shorting and thermal abuse [41], will be needed to be used alone or combined with the minichannel cooling system to prevent the thermal runaway propagation.

4. Conclusion

A novel minichannel cooling method was developed in this study for the thermal management of lithium ion batteries. The influence of the minichannel cooling on the nail penetration induced thermal runaway in li-ion battery cell and battery module was investigated. The simulation results indicate that the minichannel cooling system could not prevent the thermal runaway in a battery cell even when the flow rate is as high as 10.0 L/min. The results also show that increasing the nail penetration depth or the nail diameter will cause a more severe and faster thermal runaway. At battery module level, however, a minichannel cooling system with independent control of the coolant flow rate for individual cells can prevent the propagation of thermal runaway from one cell to its neighboring cells. When the control of the coolant flow rate is only used at battery pack level, some other techniques such as the addition of multifunctional materials into battery electrodes will be needed to be used alone or combined with the minichannel cooling system to prevent the thermal runaway propagation.

Acknowledgement

This work was funded by the United States Department of Energy under the ARPA-E program (Award No. DEAR0000396).

References

- [1] C. Lan, J. Xu, Y. Qiao, Y. Ma, Thermal management for high power lithium-ion battery by minichannel aluminum tubes, *Appl. Therm. Eng.* 101 (2016) 284–292, <http://dx.doi.org/10.1016/j.applthermaleng.2016.02.070>.
- [2] T.M. Bandhauer, S. Garimella, T.F. Fuller, A critical review of thermal issues in lithium-ion batteries, *J. Electrochem. Soc.* 158 (2011) R1–R25.
- [3] L. Lu, X. Han, J. Li, J. Hua, M. Ouyang, A review on the key issues for lithium-ion battery management in electric vehicles, *J. Power Sources* 226 (2013) 272–288.
- [4] A.A. Pesaran, Battery thermal management in EVs and HEVs: issues and solutions, in: *Advanced Automotive Battery Conference Las Vegas, Nevada, 2011*.
- [5] S. Panchal, I. Dincer, M. Agelin-Chaab, R. Fraser, M. Fowler, Thermal modeling and validation of temperature distributions in a prismatic lithium-ion battery at different discharge rates and varying boundary conditions, *Appl. Therm. Eng.* 96 (2016) 190–199.
- [6] J. Smith, M. Hinterberger, C. Schneider, J. Koehler, Energy savings and increased electric vehicle range through improved battery thermal management, *Appl. Therm. Eng.* 101 (2016) 647–656.
- [7] J.P. Rugh, A. Pesaran, K. Smith, Electric vehicle battery thermal issues and thermal management techniques, in: *SAE 2011 Alternative Refrigerant and System Efficiency Symposium, 2011*.
- [8] X. Xu, R. He, Review on the heat dissipation performance of battery pack with different structures and operation conditions, *Renew. Sustain. Energy Rev.* 29 (2014) 301–315.
- [9] T. Wang, K. Tseng, J. Zhao, Z. Wei, Thermal investigation of lithium-ion battery module with different cell arrangement structures and forced air-cooling strategies, *Appl. Energy* 134 (2014) 229–238.
- [10] S.K. Mohammadian, Y. Zhang, Thermal management optimization of an air-cooled Li-ion battery module using pin-fin heat sinks for hybrid electric vehicles, *J. Power Sources* 273 (2015) 431–439.
- [11] L. Fan, J. Khodadadi, A. Pesaran, A parametric study on thermal management of an air-cooled lithium-ion battery module for plug-in hybrid electric vehicles, *J. Power Sources* 238 (2013) 301–312.
- [12] M.R. Giuliano, A.K. Prasad, S.G. Advani, Experimental study of an air-cooled thermal management system for high capacity lithium-titanate batteries, *J. Power Sources* 216 (2012) 345–352.
- [13] N. Putra, B. Ariantara, R.A. Pamungkas, Experimental investigation on performance of lithium-ion battery thermal management system using flat plate loop heat pipe for electric vehicle application, *Appl. Therm. Eng.* 99 (2016) 784–789.
- [14] J.T. Zhao, Z.H. Rao, Y.T. Huo, X.J. Liu, Y.M. Li, Thermal management of cylindrical power battery module for extending the life of new energy electric vehicles, *Appl. Therm. Eng.* 85 (2015) 33–43.
- [15] I. Kruger, D. Limperich, G. Schmitz, Energy consumption of battery cooling in hybrid electric vehicles, in: *International Refrigeration and Air Conditioning Conference, Purdue, West Lafayette, IN, 2012*.
- [16] P. Kritzer, H. Döring, B. Emermacher, Improved safety for automotive lithium batteries: an innovative approach to include an emergency cooling element, *Adv. Chem. Eng. Sci.* 4 (2014) 197–207.
- [17] L. Jin, P. Lee, X. Kong, Y. Fan, S. Chou, Ultra-thin minichannel LCP for EV battery thermal management, *Appl. Energy* 113 (2014) 1786–1794.
- [18] Y. Zhang, X. Yu, Q. Feng, R. Zhang, Thermal performance study of integrated cold plate with power module, *Appl. Therm. Eng.* 29 (2009) 3568–3573.
- [19] Y. Huo, Z. Rao, X. Liu, J. Zhao, Investigation of power battery thermal management by using mini-channel cold plate, *Energy Convers. Manage.* 89 (2015) 387–395.
- [20] R. Kizilel, R. Sabbah, J.R. Selman, S. Al-Hallaj, An alternative cooling system to enhance the safety of Li-ion battery packs, *J. Power Sources* 194 (2009) 1105–1112.
- [21] Z. Rao, S. Wang, A review of power battery thermal energy management, *Renew. Sustain. Energy Rev.* 15 (2011) 4554–4571.
- [22] X. Duan, G.F. Naterer, Heat transfer in phase change materials for thermal management of electric vehicle battery modules, *Int. J. Heat Mass Transf.* 53 (2010) 5176–5182.
- [23] N. Javani, I. Dincer, G.F. Naterer, G.L. Rohrauer, Modeling of passive thermal management for electric vehicle battery packs with PCM between cells, *Appl. Therm. Eng.* 73 (2014) 307–316.
- [24] D.P. Finegan, M. Scheel, J.B. Robinson, B. Tjaden, I. Hunt, T.J. Mason, J. Millichamp, M. Di Michiel, G.J. Offer, G. Hinds, D.J.L. Brett, P.R. Shearing, In-operando high-speed tomography of lithium-ion batteries during thermal runaway, *Nat. Commun.* 6 (2015).
- [25] Q.S. Wang, P. Ping, X.J. Zhao, G.Q. Chu, J.H. Sun, C.H. Chen, Thermal runaway caused fire and explosion of lithium ion battery, *J. Power Sources* 208 (2012) 210–224.
- [26] D. Lisbona, T. Snee, A review of hazards associated with primary lithium and lithium-ion batteries, *Process Saf. Environ. Prot.* 89 (2011) 434–442.
- [27] A. Pesaran, S. Santhanagopalan, G.-H. Kim, Addressing the impact of temperature extremes on large format Li-ion batteries for vehicle applications, in: *30th International Battery Seminar, Ft. Lauderdale, Florida, 2013*.
- [28] S. Tobishima, J. Yamaki, A consideration of lithium cell safety, *J. Power Sources* 81 (1999) 882–886.
- [29] X.N. Feng, J. Sun, M.G. Ouyang, F. Wang, X.M. He, L.G. Lu, H.E. Peng, Characterization of penetration induced thermal runaway propagation process within a large format lithium ion battery module, *J. Power Sources* 275 (2015) 261–273.
- [30] R. Spotnitz, J. Franklin, Abuse behavior of high-power, lithium-ion cells, *J. Power Sources* 113 (2003) 81–100.
- [31] K.C. Chiu, C.H. Lin, S.F. Yeh, Y.H. Lin, K.C. Chen, An electrochemical modeling of lithium-ion battery nail penetration, *J. Power Sources* 251 (2014) 254–263.
- [32] T.D. Hatchard, D.D. MacNeil, A. Basu, J.R. Dahn, Thermal model of cylindrical and prismatic lithium-ion cells, *J. Electrochem. Soc.* 148 (2001) A755–A761.
- [33] G.H. Kim, A. Pesaran, R. Spotnitz, A three-dimensional thermal abuse model for lithium-ion cells, *J. Power Sources* 170 (2007) 476–489.
- [34] W. Zhao, G. Luo, C.Y. Wang, Modeling nail penetration process in large-format Li-ion cells, *J. Electrochem. Soc.* 162 (2015) A207–A217.
- [35] X.N. Feng, X.M. He, M.G. Ouyang, L.G. Lu, P. Wu, C. Kulp, S. Prasser, Thermal runaway propagation model for designing a safer battery pack with 25 Ah LiNi_xCo_yMn_zO₂ large format lithium ion battery, *Appl. Energy* 154 (2015) 74–91.
- [36] C. Yang, G.H. Kim, S. Santhanagopalan, A. Pesaran, Multi-physics modeling of thermal runaway propagation in a Li-ion battery module, in: *225th ECS Meeting, Orlando, FL, 2014*.
- [37] M. Chen, Q.J. Sun, Y.Q. Li, K. Wu, B.J. Liu, P. Peng, Q.S. Wang, A thermal runaway simulation on a lithium titanate battery and the battery module, *Energies* 8 (2015) 490–500.
- [38] X. Xie, Z. Liu, Y. He, W. Tao, Numerical study of laminar heat transfer and pressure drop characteristics in a water-cooled minichannel heat sink, *Appl. Therm. Eng.* 29 (2009) 64–74.
- [39] C.L. Yeh, C.Y. Wen, Y.F. Chen, S.H. Yeh, C.H. Wu, An experimental investigation of thermal contact conductance across bolted joints, *Exp. Thermal Fluid Sci.* 25 (2001) 349–357.
- [40] C. Brace, H. Burnham-Slipper, R. Wijetunge, N. Vaughan, Integrated cooling systems for passenger vehicles, *SAE Technical Paper 2001-01-1248, 2001*.
- [41] A.V. Le, M. Wang, Y. Shi, D. Noelle, Y. Qiao, W. Lu, Effects of additional multiwall carbon nanotubes on impact behaviors of LiNi_{0.5}Mn_{0.3}Co_{0.2}O₂ battery electrodes, *J. Appl. Phys.* 118 (2015) 085312.